



Effects of electrostatic interaction on clustering and collision of bidispersed inertial particles in homogeneous and isotropic turbulence

Xuan Ruan¹, Matthew T. Gorman¹ and Rui Ni^{1,†}

¹Department of Mechanical Engineering, Johns Hopkins University, Baltimore, MD 21218, USA

(Received 5 September 2023; revised 8 November 2023; accepted 6 December 2023)

In sandstorms and thunderclouds, turbulence-induced collisions between solid particles and ice crystals lead to inevitable triboelectrification. The charge segregation is usually size dependent, with small particles charged negatively and large particles charged positively. In this work, we perform numerical simulations to study the influence of charge segregation on the dynamics of bidispersed inertial particles in turbulence. Direct numerical simulations of homogeneous isotropic turbulence are performed with the Taylor Reynolds number $Re_\lambda = 147.5$, while particles are subjected to both electrostatic interactions and fluid drag, with Stokes numbers of 1 and 10 for small and large particles, respectively. Coulomb repulsion/attraction is shown to effectively inhibit/enhance particle clustering within a short range. Besides, the mean relative velocity between same-size particles is found to rise as the particle charge increases because of the exclusion of low-velocity pairs, while the relative velocity between different-size particles is almost unaffected, emphasizing the dominant roles of differential inertia. The mean Coulomb-turbulence parameter, Ct_0 , is then defined to characterize the competition between the Coulomb potential energy and the mean relative kinetic energy. In addition, a model is proposed to quantify the rate at which charged particles approach each other and to capture the transition of the particle relative motion from the turbulence-dominated regime to the electrostatic-dominated regime. Finally, the probability distribution function of the approach rate between particle pairs is examined, and its dependence on the Coulomb force is further discussed using the extended Coulomb-turbulence parameter.

Key words: multiphase flow, particle/fluid flow

† Email address for correspondence: rui.ni@jhu.edu

1. Introduction

Particle-laden turbulent flows are widespread in both nature and industry. One of the most important features of turbulence is its ability to effectively transport suspended particles and create highly inhomogeneous particle distributions, which eventually lead to frequent particle collisions or bubble/droplet coalescence (Falkovich, Gawedzki & Vergassola 2001; Toschi & Bodenschatz 2009; Pumir & Wilkinson 2016). Typical natural processes can be found as rain formation (Shaw 2003; Grabowski & Wang 2013), sandstorms (Zhang & Zhou 2020) and the formation of marine snow in the ocean (Arguedas-Leiva *et al.* 2022), while in industrial applications turbulence-induced collisions are also shown to be essential in dusty particle removal (Jaworek *et al.* 2018) and flocculation (Zhao *et al.* 2021).

It has been widely shown that the spatial distribution of inertial particles is highly non-uniform and intermittent, which is known as preferential concentration (Maxey 1987; Squires & Eaton 1991). Preferential concentration could significantly enhance the local particle number density and facilitate interparticle collisions (Reade & Collins 2000). At the dissipative range, clustering is driven by Kolmogorov-scale eddies that eject heavy particles out of high-vorticity regions while entrapping light bubbles (Balkovsky, Falkovich & Fouxon 2001; Calzavarini *et al.* 2008; Mathai *et al.* 2016). Moreover, later studies show that, in addition to clustering at the dissipative scale, the coexistence of multi-scale vortices in turbulence also affects the dynamics of heavy particles with relaxation times much larger than the Kolmogorov time scale, and drives self-similar clustering at larger scales (Goto & Vassilicos 2006; Bec *et al.* 2007; Yoshimoto & Goto 2007; Baker *et al.* 2017). Besides, the inertial-range clustering of heavy particles can be alternatively explained by the sweep-stick mechanism, where inertial particles are assumed to stick to and move with fluid elements with zero acceleration (Goto & Vassilicos 2008).

Apart from preferential concentration, the sling effect or the formation of caustics becomes more significant with the growth of particle inertia or turbulence intensity (Falkovich, Fouxon & Stepanov 2002; Wilkinson & Mehlig 2005; Wilkinson, Mehlig & Bezuglyy 2006; Falkovich & Pumir 2007). When sling happens, inertial particles encountering intermittent fluctuations get ejected out of local flow. Then, clouds of particles with different flow histories interpenetrate each other with large relative velocities (Bewley, Saw & Bodenschatz 2013). As a result, the large relative velocity gives rise to an abrupt growth of the collision frequency, and the sling effect becomes the dominant collision mechanism for large-inertia particles (Voßkuhle *et al.* 2014).

By means of direct numerical simulations (DNSs), the contributions of both preferential concentration and the sling effect (or the turbulence transport effect) to the collision rate could be quantified separately. A framework based on the radial distribution function and the mean relative velocity was proposed to predict the collision kernel function of neutral monodisperse particles with arbitrary inertia (Sundaram & Collins 1997; Wang, Wexler & Zhou 2000). Based on this framework, the impacts of turbulence Reynolds number, nonlinear drag, gravity and hydrodynamic interactions were systematically investigated (Ayala, Rosa & Wang 2008*a*; Ayala *et al.* 2008*b*; Ireland, Bragg & Collins 2016*a,b*; Ababaei *et al.* 2021; Bragg *et al.* 2022). In addition to monodisperse particles, this framework was also extended to bidispersed particle systems. Compared with monodisperse system, the clustering of different-size particles is found to be weaker, while the turbulent transport effect is more pronounced due to the particles' different responses to turbulent fluctuations (Zhou, Wexler & Wang 2001).

In addition to neutral particles, particles in nature could easily get charged after moving through ionized air (Marshall & Li 2014; van Minderhout *et al.* 2021) or encountering collisions (Lee *et al.* 2015). The resulting electrostatic interaction could significantly

modulate the fundamental particle dynamics in turbulence, such as clustering, dispersion and agglomeration (Karnik & Shrimpton 2012; Yao & Capecelatro 2018; Ruan, Chen & Li 2021; Boutsikakis, Fede & Simonin 2022; Ruan & Li 2022; Zhang, Cui & Zheng 2023). For identically charged particles, it has been shown that the Coulomb repulsion could effectively repel close particle pairs and mitigate particle clustering. By assuming that the drift velocity caused by the Coulomb force can be superposed on the turbulence drift velocity, the radial distribution function of particles with negligible/finite inertia can be derived, which shows good agreement with both experimental and numerical results (Lu *et al.* 2010*a*; Lu, Nordsiek & Shaw 2010*b*; Lu & Shaw 2015).

Different from the like-charged monodisperse system, real charged particle-laden flows may be more complicated because: (i) the size of suspended particles is generally polydispersed (Zhang & Zhou 2020), and (ii) the charge polarity varies with the particle size because of charge segregation. That is, after triboelectrification, smaller particles tend to accumulate negative charges while large ones are preferentially positively charged (Forward, Lacks & Sankaran 2009; Lee *et al.* 2015). In the previous work by Di Renzo & Urzay (2018), DNS of the bidispersed suspensions of oppositely charged particles was performed. It was shown that the aerodynamic response of different-size particles to turbulent fluctuations varies significantly. Although the system is overall neutral, different clustering behaviours lead to a spatial separation of positive and negative charge generating mesoscale electric fields in space.

However, even though the charge segregation is often correlated with the size difference, few studies have been devoted to the dynamics of bidispersed particles with both charge and size differences. In this system, three kinds of electrostatic interactions are introduced simultaneously, i.e. repulsion between small–small/large–large particles and attraction between small–large particles. How these electrostatic forces affect the clustering of bidispersed particles is less understood. Moreover, the collision frequency of charged particles is of great importance to understand the physics of rain initiation (Harrison *et al.* 2020) and planet formation (Steinpilz *et al.* 2020), and the influence of charge segregation on these processes are still unclear.

To address the above issues, in this study we perform DNSs to investigate the dynamics of bidispersed oppositely charged particles in homogeneous isotropic turbulence. The numerical methods are introduced in § 2. In § 3, the statistics of the radial distribution function and the mean relative velocity are first presented to show the effects of the electrostatic force on the clustering and the relative motion between different kinds of particle pairs. Then, the modulation of collision frequency is quantified using the particle flux, and the mean Coulomb-turbulence parameter is proposed to characterize the relative importance of the electrostatic force compared with particle–turbulence interaction. Finally, the particle flux density in the relative velocity space is discussed, which illustrates in detail how the electrostatic force affects the collision of charged particle pairs with different relative velocities.

2. Methods

2.1. Simulation conditions

The transport of bidispersed solid particles in turbulence is numerically investigated using the Eulerian–Lagrangian framework. The flow field is homogeneous isotropic turbulence with the Taylor Reynolds number $Re_\lambda = 147.5$. Solid particles are treated as discrete points and their motions are updated based on the Maxey–Riley equation (Maxey & Riley 1983).

Parameters	Values	Units
Flow properties		
Domain size, L	$2\pi \times 10^{-2}$	m
Grid number, N_{grid}^3	192^3	—
Taylor Reynolds number, Re_λ	147.5	—
Fluid density, ρ_f	1.0	kg m^{-3}
Fluid kinetic viscosity, ν_f	1×10^{-5}	$\text{m}^2 \text{s}^{-1}$
Fluctuation velocity, u'	0.587	m s^{-1}
Dissipation rate, ϵ	8.18	$\text{m}^2 \text{s}^{-3}$
Kolmogorov length scale, η	1.05×10^{-4}	m
Kolmogorov time scale, τ_η	1.11×10^{-3}	s
Integral length scale, L_{int}	9.08×10^{-3}	m
Eddy turnover time, τ_e	1.547×10^{-2}	s
Particle properties		
Particle density, ρ_p	1984.5	kg m^{-3}
Particle diameter, $d_{p,S}/d_{p,L}$	10/31.6	μm
Particle charge, q	$\{0, 0.5, 1, 2\} \times 10^{-14}$	C
Particle number, $N_{p,S}/N_{p,L}$	$10^5/10^5$	—
Particle volume fraction, ϕ_{par}	6.87×10^{-6}	—

Table 1. Simulation parameters.

Table 1 lists the simulation parameters used in this study. Particle properties are chosen based on typical values of silica particles suspended in gaseous turbulence. Here, the particle density is much larger than that of the air ($\rho_p/\rho_f \sim O(10^3)$), and the particle size is smaller than the Kolmogorov length (i.e. $d_{p,S}/\eta = 0.1$, $d_{p,L}/\eta \approx 0.3$, where $d_{p,S}$ and $d_{p,L}$ are the diameters of small and large particles, respectively, and η is the Kolmogorov length scale). The particle Stokes number St , defined as the ratio of the particle relaxation time τ_p to the Kolmogorov time scale τ_η , is given by

$$St = \frac{\tau_p}{\tau_\eta} = \frac{1}{18} \frac{\rho_p}{\rho_f} \left(\frac{d_p}{\eta} \right)^2. \quad (2.1)$$

In previous field measurements (Zhang & Zhou 2020), the Stokes number of sand particles was mainly in the range of $St = 1$ –10 in strong sandstorms. We thus choose $St_S = 1$ and $St_L = 10$ as the typical Stokes numbers for small and large particles, respectively. In addition, since the measured particle mass concentration in Zhang & Zhou (2020) is low, the particle volume fraction is set small ($\phi_{par} = 6.87 \times 10^{-6}$) in our simulation, and the force feedback from the dilute particle phase to the fluid phase is omitted (Balachandar & Eaton 2010).

When choosing the particle charge, we assume that particles carry a certain amount of charge as a result of triboelectrification. Both small and large particles are assigned the same amount of charge q but with the opposite polarities. Because of charge segregation, small particles ($St_S = 1$) are negatively charged while large particles ($St_L = 10$) are positive. In previous measurements of tribocharged particles, the surface charge density could reach $\sigma_p \approx 10^{-5} \mu\text{C m}^{-2}$ (Waitukaitis *et al.* 2014; Lee *et al.* 2015; Harper *et al.* 2021). For a particle size of $d_p \sim 10 \mu\text{m}$, the order of the particle charge can be estimated as $q = \pi d_p^2 \sigma_p \sim 10^{-14} \text{C}$. Moreover, since the considered particle concentration is low,

particle collision is negligible. So the charge transfer is not included and the prescribed charge on each individual particle remains constant.

2.2. Fluid phase

The DNS of the incompressible homogeneous isotropic turbulence is performed using the pseudo-spectral method. The computation domain is a triply periodic cubic box with the domain size $L^3 = (2\pi \times 10^{-2} \text{ m})^3$ and the grid number $N_{grid}^3 = 192^3$. The governing equations of the fluid phase are given by

$$\nabla \cdot \mathbf{u} = 0, \tag{2.2}$$

and

$$\frac{\partial \mathbf{u}}{\partial t} + \mathbf{u} \cdot \nabla \mathbf{u} = -\frac{1}{\rho_f} \nabla p + \nu_f \nabla^2 \mathbf{u} + \mathbf{f}_F. \tag{2.3}$$

Here, $\mathbf{u}(x_i)$ is the fluid velocity at the grid node x_i , p is the pressure, ρ_f is the fluid density and ν_f is the fluid kinematic viscosity; \mathbf{f}_F is the forcing term that injects kinetic energy from large scales and keeps the turbulence steady. In the wavenumber space, the forcing term is given by

$$\hat{\mathbf{f}}_F(\boldsymbol{\kappa}) = \begin{cases} C\hat{\mathbf{u}}(\boldsymbol{\kappa}), & |\boldsymbol{\kappa}| \leq \kappa_{crit} \\ 0, & |\boldsymbol{\kappa}| > \kappa_{crit} \end{cases}. \tag{2.4}$$

Here, C is the constant forcing coefficient, the critical wavenumber is $\kappa_{crit} = 5\kappa_0$ with $\kappa_0 = 2\pi/L$ the smallest wavenumber.

When evolving the turbulence, the second-order Adam–Bashforth scheme is used for the nonlinear term while the viscous term is integrated exactly (Vincent & Meneguzzi 1991). The fluid time step is $\Delta t_F = 1 \times 10^{-5}$ s. Table 1 lists typical parameters of the homogeneous and isotropic turbulence. The fluctuation velocity u' and the dissipation rate ϵ can be obtained from the energy spectrum $E(\kappa)$ as

$$\frac{3}{2}u'^2 = \int_{\kappa_{min}}^{\kappa_{max}} E(\kappa) d\kappa, \quad \epsilon = \int_{\kappa_{min}}^{\kappa_{max}} 2\nu\kappa^2 E(\kappa) d\kappa. \tag{2.5a,b}$$

The Kolmogorov length and time scales are given by $\eta = (\nu_f^3/\epsilon)^{1/4}$ and $\tau_\eta = (\nu_f/\epsilon)^{1/2}$, respectively. The integral length scale is $l = (\pi/2u'^2) \int_{\kappa_{min}}^{\kappa_{max}} [E(\kappa)/\kappa] d\kappa$, the eddy turnover time is $\tau_e = l/u'$ and the Taylor Reynolds number is $Re_\lambda = u'\lambda/\nu_f$, with $\lambda = u'(15\nu_f/\epsilon)^{1/2}$ the Taylor microscale.

2.3. Particle motion

The movements of charged particles are integrated using the second-order Adam–Bashforth time stepping. The particle time step is $\Delta t_p = 2.5 \times 10^{-6}$ s. This time step is much smaller than the particle relaxation time to well resolve the particles' aerodynamic response to the turbulence ($\Delta t_p/\tau_{p,S} = 0.23\%$). Besides, within each step, particles only move a short distance compared with the Kolmogorov length ($u'\Delta t_p/\eta = 1.4\%$), so that the variation of the electrostatic force is well captured when particles become close. The governing

equations of particle motions are

$$m_i \frac{d\mathbf{v}_i}{dt} = \mathbf{F}_i^F + \mathbf{F}_i^E, \tag{2.6a}$$

$$\frac{d\mathbf{x}_i}{dt} = \mathbf{v}_i. \tag{2.6b}$$

Here, \mathbf{v}_i and \mathbf{x}_i are the velocity and the location of particle i , respectively; $m_i = \pi\rho_p d_{p,i}^3/6$ is the particle mass, with ρ_p the density and $d_{p,i}$ the diameter; \mathbf{F}_i^F and \mathbf{F}_i^E are the fluid force and the electrostatic force acting on particle i .

Since particles are small ($d_p < \eta$) and heavy ($\rho_p/\rho_f \gg 1$), the dominant fluid force comes from the Stokes drag (Maxey & Riley 1983)

$$\mathbf{F}_i^F = -3\pi\mu_f d_p (\mathbf{v}_i - \mathbf{u}(\mathbf{x}_i)). \tag{2.7}$$

Here, μ_f is the dynamic viscosity of the fluid, and $\mathbf{u}(\mathbf{x}_i)$ is the fluid velocity at the particle position. For two consecutive particle time steps within the same fluid time step, the flow field remains unchanged, and the fluid velocity at the particle location is interpolated at each particle time step using the second-order tri-linear interpolation scheme (Marshall 2009; Qian, Ruan & Li 2022). The effect of fluid inertia is neglected by assuming that the particle Reynolds number Re_p is much smaller than unity.

In this dilute system, the average separation between charged particles is large compared with the particle size ($\bar{l} \gg d_p$), indicating an insignificant effect of particle polarization (Ruan *et al.* 2022). Therefore, the electrostatic force acting on each particle i can be obtained by summing the pairwise Coulomb force from other particles j , which reads

$$\mathbf{F}_i^E = \sum_{j \neq i} \frac{q_i q_j (\mathbf{x}_i - \mathbf{x}_j)}{4\pi\epsilon_0 |\mathbf{x}_i - \mathbf{x}_j|^3}. \tag{2.8}$$

Here, $\epsilon_0 = 8.8542 \times 10^{-12} \text{ F m}^{-1}$ is the vacuum permittivity, q_i is the point charge located at the centroid of particle i .

To properly apply the periodic boundary condition of the long-range electrostatic force, several layers of image domains are added around the original computation domain (Di Renzo & Urzay 2018; Boutsikakis, Fede & Simonin 2023). When calculating the electrostatic force acting on the i th particle located at \mathbf{x}_i , the contributions from other particles j at \mathbf{x}_j as well as their images at $\mathbf{x}_j + (li + mj + nk)L$ are all considered

$$\mathbf{F}_i^E = \sum_{j \neq i} \sum_{l,m,n} \frac{q_i q_j \{\mathbf{x}_i - [\mathbf{x}_j + (li + mj + nk)L]\}}{4\pi\epsilon_0 |\mathbf{x}_i - [\mathbf{x}_j + (li + mj + nk)L]|^3}, \tag{2.9}$$

where $l, m, n = -N_{per}, \dots, N_{per}$. Here, \mathbf{i}, \mathbf{j} and \mathbf{k} are unit vectors along the x, y and z directions.

According to (2.9), when computing the electrostatic force acting on the target particle i , the cost is $O(N_s) = O((N_p - 1) \times (2N_{per} + 1)^3)$, where $O(N_s)$ is the number of source particles to each target particle. The total cost of the electrostatic computation then scales with $O(N_p^2 N_{per}^3)$. Considering the large particle number and the addition of image domains, direct summation (2.9) is extremely expensive. Therefore, we employ the fast multipole method (FMM) to accelerate the calculation. In FMM, the field strength generated by neighbouring particles is directly computed using (2.9), while the contribution from clouds of particles far from the target particle is approximated using fast multipole expansion,

which reduces the required computation cost to $O(N_p \log(N_p N_{per}^3))$ (Greengard & Rokhlin 1987, 1997). In this study, the open-source library FMMLIB3D is employed to conduct the fast electrostatic computation (Gimbutas & Greengard 2015). The accuracy of FMM with various layers of image domains is compared in Appendix A. Based on the analysis, two layers of image boxes ($N_{per} = 2$) are added, which is sufficient to ensure the convergence of the electrostatic force acting on all particles in the original domain.

Moreover, the Coulomb force is capped if the distance between two particles is smaller than a preset critical distance to avoid a non-physically strong force

$$F_{i \leftarrow j}^E = \min \left\{ \frac{q_i q_j}{4\pi\epsilon_0 |\mathbf{x}_i - \mathbf{x}_j|^2}, \frac{q_i q_j}{4\pi\epsilon_0 d_{cap}^2} \right\}. \quad (2.10)$$

Here, the critical distance is $d_{cap} = d_{p,SS}/2$ or $d_{cap} = \eta/20$. This value is chosen so that, even for a pair of small particles approaching each other, the Coulomb force between them is still accurate at the collision distance ($|\mathbf{x}_i - \mathbf{x}_j| = d_{p,SS} > d_{cap}$). Moreover, since d_{cap} is set small compared with the Kolmogorov length scale η , capping the electrostatic force does not affect the statistics at larger scales presented below.

In each run, the single-phase turbulence is first evolved until reaching the steady state. Particles are then injected randomly in the domain with their initial velocities equal to the fluid velocity at particle locations. It takes roughly $3.5\tau_e$ for particle dynamics to reach equilibrium, statistics are then taken over another $5\tau_e$. Three parallel runs with different initial particle locations are performed for each case, and their results are averaged and presented below.

3. Results and discussions

3.1. Clustering and relative velocity of charged particles

Figure 1 compares the spatial distribution of bidispersed particles within a thin slice $|z| \leq 20\eta$. Although oppositely charged bidispersed particles are simulated in each case, we show small and large particles in the left and the right panels separately for better illustration. In the neutral case (figure 1a,b), particle behaviour is solely determined by the particle–turbulence interaction. Small particles ($St = 1$) are responsive to fluctuations at the Kolmogorov length scale. As a result, their spatial distribution is highly non-uniform, and small-scale particle clusters can be observed (figure 1a). Meanwhile, large particles ($St = 10$) are more inertial, so they are more dispersed in the domain (figure 1b).

We employ the radial distribution function (RDF) to quantify how particles from the same (or different) size groups cluster. The RDFs of different kinds of particle pairs, i.e. small–small (SS), large–large (LL) and small–large (SL) pairs, are defined as

$$g_{SS}(r) = \frac{\Delta N_{SS}(r)/\Delta V(r)}{N_{p,S}(N_{p,S} - 1)/2/L^3}, \quad g_{LL}(r) = \frac{\Delta N_{LL}(r)/\Delta V(r)}{N_{p,L}(N_{p,L} - 1)/2/L^3}, \quad (3.1a)$$

$$g_{SL}(r) = \frac{\Delta N_{SL}(r)/\Delta V(r)}{N_{p,S}N_{p,L}/L^3}. \quad (3.1b)$$

In the definition of $g_{SS}(r)$, $\Delta N_{SS}(r)$ is the number of SS pairs with separation distances within the range of $r \pm \Delta r/2$, and $\Delta V(r) = 4\pi[(r + \Delta r/2)^3 - (r - \Delta r/2)^3]/3$ is the shell volume in the separation distance bin; $N_{p,S}(N_{p,S} - 1)/2/L^3$ is the average number of SS pairs in the whole domain. Therefore, $g_{SS}(r) > 1$ means there is a higher density of

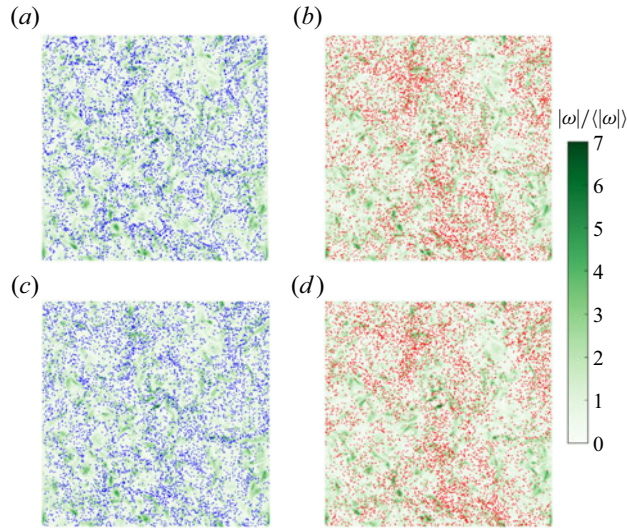


Figure 1. Snapshots of particles in the slice $|z| \leq 20\eta$ with (a) $St = 1$ and $q = 0$ C, (b) $St = 10$ and $q = 0$ C, (c) $St = 1$ and $q = 2 \times 10^{-14}$ C, (d) $St = 10$ and $q = 2 \times 10^{-14}$ C. Blue/red dots represent small/large particles. The colour bar indicates the vorticity magnitude normalized by its average over the domain.

SS pairs at a given separation distance of r compared with the average pair density. The definitions of $g_{LL}(r)$ and $g_{SL}(r)$ are similar and thus omitted.

As shown in figure 2(a), $g_{SS}(r)$ for neutral pairs is significantly larger than unity at $r \leq \eta$, indicating strong clustering at the small scale; $g_{SS}(r)$ also follows a clear power law $g_{SS}(r) \sim (r/\eta)^{-c_1}$ with the fitted exponent $c_1 = 0.69$. The value of c_1 is close to those reported in previous studies with similar Re_λ , e.g. $c_1 = 0.67$ for $Re_\lambda = 143$ (Saw *et al.* 2012) and $c_1 = 0.68$ for $Re_\lambda = 140$ (Ireland *et al.* 2016a). In comparison, $g_{LL}(r)$ for neutral pairs is only slightly larger than one, which means the clustering of large particles is relatively weak. However, $g_{LL}(r)$ decreases slowly with the increase of r and stays above unity until $r \approx 100\eta$, while $g_{SS}(r)$ drops rapidly and approaches unity around $20\text{--}30\eta$. This is because the clustering of inertial particles with the relaxation time τ_p is driven by vortices whose time scales are comparable to a particle's relaxation time (i.e. $\tau(r) \sim \tau_p$). In the inertial range, the time scale satisfies $\tau(r) \sim \epsilon^{-1/3} r^{2/3}$, so the relationship can be given as $r \sim \epsilon^{1/3} \tau_p^{3/2}$ (Yoshimoto & Goto 2007; Bec *et al.* 2011). With the increase of particle inertia, the length and the time scales of vortices that could affect particle behaviours also become larger. As a result, the size of particle clusters also grow larger, leading to the large correlation length in $g_{LL}(r)$ (Yoshimoto & Goto 2007; Liu *et al.* 2020). Besides, when comparing those particles with a large St difference, because their relaxation times differ by a factor of ten, they respond to flows of very different scales. Therefore, there is little spatial correlation between small and large particles, and $g_{SL}(r)$ is close to unity at all separation distance r when particles are neutral.

When particles are charged, since charge segregation correlates with size, the same-size particles will repel each other when they get close. Since the amount of particle charge is the same, the effect of repulsion is more drastic between SS pairs rather than between LL pairs. As a result, the order of $g_{SS}(r)$ at small r drops by several decades as q increases. The same decreasing trend is observed for $g_{LL}(r)$, but the influence is less significant because of the large particle inertia. This can also be shown by comparing the top and the bottom panels in figure 1. In the charged case ($q = 2 \times 10^{-14}$ C), the small particles become less

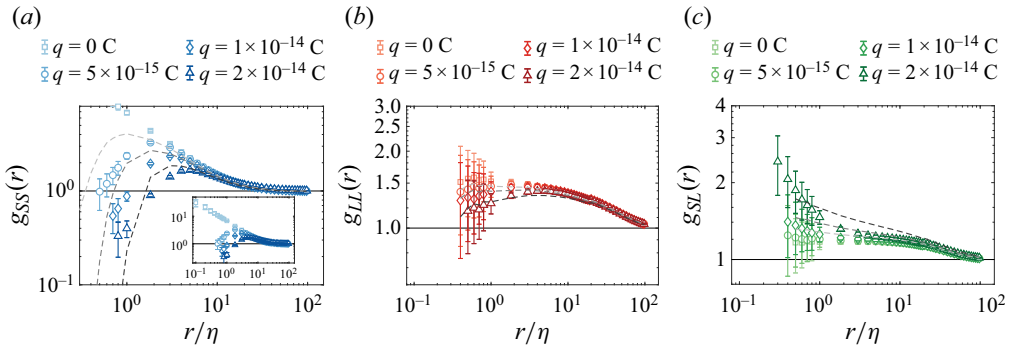


Figure 2. The RDFs between (a) SS, (b) LL and (c) SL particle pairs with different particle charge q . The inset in (a) shows the full scale of $g_{SS}(r)$ in the neutral case. Dashed lines from light to dark correspond to predicted RDFs using (3.12) (or its counterpart for the oppositely charged case) for $q = 5 \times 10^{-15}$ C, 1×10^{-14} C and 2×10^{-14} C, respectively.

concentrated (figure 1c), while no obvious difference is seen in the spatial distribution of large particles (figure 1d). It is worth noting that, since the Coulomb force decays rapidly with r , its effect is only significant within a relatively short range ($r \approx 1-10\eta$). Beyond this range, both $g_{SS}(r)$ and $g_{LL}(r)$ in figure 2(a,b) recover to their neutral values again, so clustering could still be observed at large r . As for g_{SL} , because of the Coulomb attraction, particles of different sizes are more likely to stay close. More specifically, considering the large mass difference between SL pairs ($m_L/m_S = (St_L/St_S)^{1.5} \approx 30$), small particles will always be attracted towards the large ones, giving rise to the rapid growth of $g_{SL}(r)$ at small separation ($r \leq \eta$). Again, the opposite-sign attraction decays with increasing r , so $g_{SL}(r)$ approaches one when r is sufficiently large.

Apart from spatial correlation, it is also of interest to study the relative velocity between particle pairs and focus on the modulation caused by the electrostatic force. For a pair of particles i and j with the separation $r = |\mathbf{x}_i - \mathbf{x}_j|$, the radial component of the relative velocity is defined as $w_{r,ij} = (\mathbf{v}_i - \mathbf{v}_j) \cdot (\mathbf{x}_i - \mathbf{x}_j) / |\mathbf{x}_i - \mathbf{x}_j|$. Taking the ensemble average over SS/LL/SL particle pairs then yields the mean relative velocities between three kinds of particle pairs as $\langle |w_{r,SS}| \rangle$, $\langle |w_{r,LL}| \rangle$ and $\langle |w_{r,SL}| \rangle$, respectively.

Figure 3(a) compares the mean radial relative velocity between SS pairs, $\langle |w_{r,SS}| \rangle$, for various particle charge q . For neutral SS pairs, when r is in the inertial range ($\eta \ll r \ll L_{int}$), $\tau_{p,S}$ is much smaller than the characteristic time scales of turbulent fluctuations at this length scale. The radial relative velocity between SS pairs, $\langle |w_{r,SS}| \rangle$, thus follows that of fluid tracers δu_r . Here, the fluid relative velocity is obtained from the second-order longitudinal structure function as $\delta u_r = C_2^{1/2} \epsilon^{1/3} r^{1/3}$ and the constant is $C_2 = 2.13$ (Yeung & Zhou 1997) (shown as dash-dotted lines in figure 3). If r is within the dissipative range, the time scale of local fluctuations becomes comparable to $\tau_{p,S}$. Small neutral particles cannot perfectly follow the background flow at this separation, so $\langle |w_{r,SS}| \rangle$ deviates from the fluid relative velocity $\delta u_r = (\epsilon/15\nu)^{1/2} r$ (dashed lines in figure 3).

When particles are charged, since the influence of Coulomb force is negligible at large r , curves for different q collapse. In contrast, $\langle |w_{r,SS}| \rangle$ is found to rise significantly as particles get close to each other. When q gets larger, the increase of $\langle |w_{r,SS}| \rangle$ becomes more pronounced and the deviation from the neutral result also occurs at a larger r . This seems counter-intuitive because the Coulomb repulsion between SS pairs should always slow approaching particles down and reduce the relative velocity. One explanation for this change is as follows. When q is large, the strong Coulomb repulsion causes biased

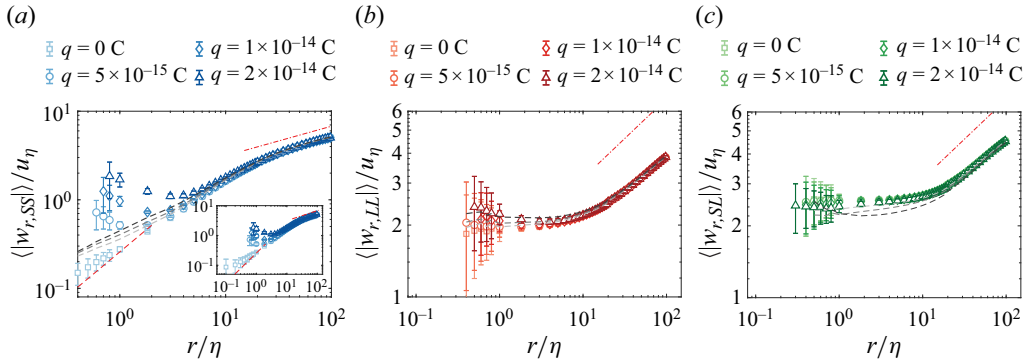


Figure 3. Mean radial relative velocity $\langle |w_{r,ij}| \rangle$ normalized by u_η between (a) SS, (b) LL and (c) SL particle pairs with different particle charge q . The inset in (a) shows the full scale of $\langle |w_{r,SS}| \rangle$ in the neutral case. The red dashed line denotes the velocity scaling $\propto r$ in the dissipation range, and the red dash-dotted line denotes the velocity scaling $\propto r^{1/3}$ in the inertial range. Dashed lines from light to dark correspond to predictions using (3.15) (or its counterpart for the oppositely charged case) for $q = 5 \times 10^{-15}$ C, 1×10^{-14} C and 2×10^{-14} C, respectively.

sampling at small r : only those pairs with large inward relative velocity could overcome the energy barrier and get close. Meanwhile, since the electrical potential energy is conserved in the approach-then-depart process, the pairs approaching each other at a high velocity will also be repelled at a high velocity as the electrostatic force pushes them apart. As a result, pairs with a large $|w_{r,SS}|$ take a large proportion of the close pairs as q increases, so the mean radial relative velocity between both approaching and departing pairs, $\langle w_{r,ij} \rangle$, shows the increasing trend in figure 3(a). This increasing trend with q will be further discussed in § 3.3.

Compared with small particles with $St = 1$, large particles with $St = 10$ are very inertial and insensitive to fluctuations even at large separations. The curves of $\langle |w_{r,LL}| \rangle$ are therefore much flatter. Besides, the constant relative velocity between LL pairs at small r is also significantly larger, because their relative velocity comes from the energetic large-scale motions. When particles are charged, the same increasing trend with q is also observed but is less significant, which can be attributed to the large kinetic energy compared with the electrostatic potential energy.

As for SL pairs, $\langle |w_{r,SL}| \rangle$ is larger than both $\langle |w_{r,SS}| \rangle$ and $\langle |w_{r,LL}| \rangle$ in the neutral cases. This is caused by the different responses of small/large particles to turbulent fluctuations, which is termed the differential inertia effect (Zhou *et al.* 2001). Interestingly, there is no obvious change when comparing curves between different charges q in figure 3(c). As shown in figure 2(c), the Coulomb force attracts small particles towards large ones and enhances their spatial correlation. Nevertheless, even though charged SL pairs experience a more similar flow history than neutral SL pairs, they will still develop large relative velocities over time because their response to local fluctuations is very different. Therefore, the influence of charge on $\langle |w_{r,SL}| \rangle$ is weak.

3.2. Effect of Coulomb force on particle flux

Once the RDF and the radial relative velocity are known, we could further investigate the collision frequency between charged particles. For a steady system, the collision frequency can be measured by the kinematic collision kernel function as (Sundaram & Collins 1997;

Wang *et al.* 2000)

$$\Gamma_{ij}(R_C) = 2\pi R_C^2 \cdot g_{ij}(R_C) \cdot \langle |w_{r,ij}| \rangle(R_C). \quad (3.2)$$

Here, $R_C = r_i + r_j$ is the collision radius, which equals the sum of the radii of particles i and j ; $g_{ij}(R_C)$ is the RDF at $r = R_C$, and the mean relative velocity is $\langle |w_{r,ij}| \rangle = \int_{-\infty}^{\infty} |w_{r,ij}| p_{ij}(w_{r,ij}) dw_{r,ij}$, with $p_{ij}(w_{r,ij})$ the probability density function (PDF) of $w_{r,ij}$ at $r = R_C$.

Even though other particle parameters (e.g. the Stokes number) are set the same, different choices of R_C will affect the final outcome of Γ_{ij} by changing the collision geometry. Therefore, instead of directly using Γ_{ij} , we define the particle flux Φ_{ij} as the ratio of the collision kernel $\Gamma_{ij}(r)$ to the area of the collision sphere $4\pi r^2$ at r as

$$\Phi_{ij}(r) = \frac{\Gamma_{ij}(r)}{4\pi r^2} = \frac{1}{2} g_{ij}(r) \cdot \langle |w_{r,ij}| \rangle(r). \quad (3.3)$$

Here, Φ_{ij} can be understood as the number of particles crossing the collision sphere per area per unit time, which is independent of the prescribed R_C .

Apart from (3.3) that uses information of both approaching and departing pairs, the particle flux can also be defined using only the approaching or departing pairs. In real situations, it is the approaching pairs that lead to collisions, so a natural way to define particle flux is based on the inward flux as

$$\Phi_{ij}^{in}(r) = g_{ij}(r) F(w_{r,ij} < 0|r) \cdot \langle w_{r,ij}^- \rangle(r). \quad (3.4)$$

Here, $F(w_{r,ij} < 0|r)$ is the fraction of particles moving inwards at r , and the mean inward relative velocity is $\langle w_{r,ij}^- \rangle = -\int_{-\infty}^0 w_{r,ij} p_{ij}(w_{r,ij}) dw_{r,ij}$. After the system reaches equilibrium, RDFs between particle pairs no longer change, suggesting that the inward flux should balance the outward flux at all r . Here, the outward particle flux is

$$\Phi_{ij}^{out}(r) = g_{ij}(r) F(w_{r,ij} > 0|r) \cdot \langle w_{r,ij}^+ \rangle(r), \quad (3.5)$$

with the mean outward relative velocity given by $\langle w_{r,ij}^+ \rangle = \int_0^{\infty} w_{r,ij} p_{ij}(w_{r,ij}) dw_{r,ij}$. The definition of Φ_{ij} is based on a pair of particles i and j without specifying their sizes. If the average is taken over all SS pairs, the result is the SS particle flux denoted by Φ_{SS} . The flux between LL pairs (Φ_{LL}) and SL pairs (Φ_{SL}) can also be obtained by taking the average over corresponding particle pairs.

The SS fluxes Φ_{SS} defined by (3.3), (3.4) and (3.5) are first compared and show good agreement with each other, indicating that the flux-balance condition is valid. Since (3.3) uses the information of both approaching and departing particle pairs, it is adopted in the following sections for better statistics.

Figure 4(a) compares the SS fluxes with various q . The flux for neutral pairs remain constant when r is comparable to η . This indicates that, although both g_{SS} (figure 2a) and $\langle |w_{r,SS}| \rangle$ (figure 3a) keep changing as r decreases, their product is almost constant for small r . For inertial particle pairs with small r , it has been shown that $g(r) \propto r^{D_2-3}$, with D_2 the correlation dimension (Bec *et al.* 2007), while the relative velocity follows $\langle w_{r,SS} \rangle \propto r^{3-D_2}$ (Gustavsson & Mehlig 2014). Therefore, the dependence of Φ_{SS} on r is cancelled out. Besides, in practical situations the collision diameter R_C between micron particles/droplets is smaller than η , so the constant flux at such separation distance leads to a quadratic dependence of collision kernel on R_C as $\Gamma_{SS} = 4\pi R_{C,SS}^2 \Phi_{SS}(R_{C,SS})$ (Sundaram & Collins 1997).

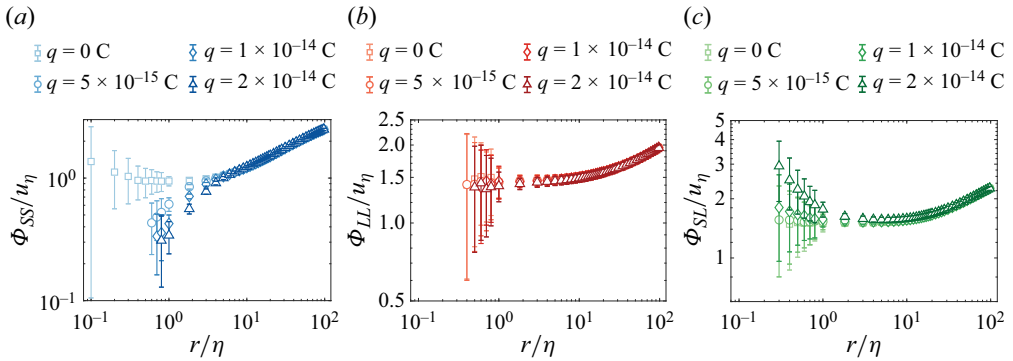


Figure 4. Particle fluxes between (a) SS, (b) LL and (c) SL particle pairs with different particle charge q .

When particles are charged, the SS flux is found to decrease rapidly as r drops. To characterize the effect of Coulomb force on the reduction of Φ_{SS} , we need to quantify the competition between the driving force and the resistance of particle collisions. For a pair of same-sign particles i and j separated by r , the driving force can be evaluated by the relative kinetic energy $E_{Kin}(r) = m_{ij}\langle|w_{r,ij}|\rangle^2/2$. Here, $m_{ij} = (m_i^{-1} + m_j^{-1})^{-1}$ is the effective mass, $\langle|w_{r,ij}|\rangle(r)$ is the mean radial relative velocity between neutral pairs with a separation of r . The resistance is the electrical energy barrier $E_{Coul} = qi q_j/4\pi\epsilon_0 r$. The energy ratio is then given as

$$Ct_0 \equiv \frac{E_{Coul}}{E_{Kin}} = \frac{qi q_j}{2\pi\epsilon_0 r m_{ij}\langle|w_{r,ij}|\rangle^2}. \tag{3.6}$$

Note that, in previous studies regarding the clustering of charged particles with weak inertia (Lu *et al.* 2010a,b), the approaching velocity between particle pairs can be directly derived through perturbation expansion in the Stokes number (Chun *et al.* 2005). In this work, however, particles are very inertial, so the mean relative velocity $\langle|w_{r,ij}|\rangle$ between neutral pairs is used instead. By using the corresponding effective mass (e.g. $m_{SS} = m_S/2$, $m_{LL} = m_L/2$, and $m_{SL} = m_S m_L/(m_S + m_L)$) and the mean relative velocity ($\langle|w_{r,SS}|\rangle$, $\langle|w_{r,LL}|\rangle$, and $\langle|w_{r,SL}|\rangle$), (3.6) can quantify the Coulomb-turbulence competition for different kinds of particle pairs. Since Ct_0 measures the relative importance of the Coulomb force to the mean relative kinetic energy, it is called the mean Coulomb-turbulence parameter hereinafter.

According to the definition in (3.6), the value of Ct_0 can be varied as the particle charges or the separation distance changes. Therefore, for each data point in figure 4(a), we plot the ratio of $\Phi_{SS}(q)$ to its corresponding value in the neutral case $\Phi_{SS}(q = 0)$ as a function of Ct_0 in figure 5(a). The flux ratios for different q are found to follow the same trend. The particle flux of charged particles is almost unaffected when Ct_0 is small, and a significant decay is observed when Ct_0 exceeds unity. The LL fluxes Φ_{LL} in figure 4(b) are analysed in a similar way, and the results are plotted in figure 5(b). Because of the large kinematic energy between LL pairs, the Coulomb repulsion is relatively weak ($Ct_0 < 1$), so the reduction of Φ_{LL} has not yet reached the electrostatic-dominant regime. As for the flux between SL pairs shown in figure 4(c), the opposite trend is seen when plotting the flux ratio as a function of Ct_0 (figure 5c). The increase of Φ_{SL} becomes significant when Ct_0 becomes larger than one.

We now propose a model to quantify the influence of the electrostatic force on the mean particle flux. For particle pairs with a separation distance r , the mean radial relative

Charged bidispersed particles in turbulence

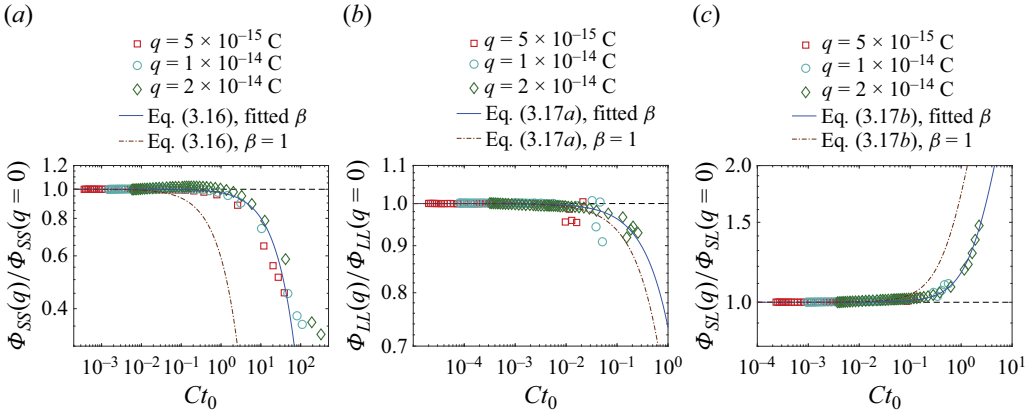


Figure 5. Ratios of charged particle flux $\Phi(q)$ to neutral particle flux $\Phi(q = 0)$ as a function of the mean Coulomb-turbulence parameter Ct_0 for (a) SS, (b) LL and (c) SL particle pairs. Blue solid lines are model predictions from (3.16) and (3.17) with fitted β . Brown dash-dotted lines are predictions with the fixed $\beta = 1$.

velocities between different kinds of particle pairs have been shown in figure 3. We then assume that, for each kind of particle pair, the relative velocity between neutral pairs follows the Gaussian distribution. Taking SS particle pairs as an example, the PDF $p_{r,SS}$ of the relative velocity $w_{r,SS}(r)$ is

$$p_{r,SS}(w_{r,SS}) = \frac{1}{\sqrt{2\pi}\sigma_{SS}} \exp\left(-\frac{w_{r,SS}^2}{2\sigma_{SS}^2}\right). \quad (3.7)$$

The standard deviation is determined by the mean relative velocity at r as $\sigma_{SS} = \sqrt{\pi/2} \cdot \langle |w_{r,SS}| \rangle(r)$. It should be noted that the relative velocity distribution is actually non-Gaussian (Sundaram & Collins 1997; Wang *et al.* 2000; Ireland *et al.* 2016a). However, a Gaussian distribution is sufficient for the first-order assumption, and has already been applied in previous studies (Pan & Padoan 2010; Lu & Shaw 2015).

We then evaluate the RDF of charged pairs. For neutral SS pairs, all particle pairs with an inward relative velocity ($w_{r,SS} < 0$) could approach each other. In comparison, when they are identically charged, only those SS pairs whose inward relative velocity exceeds a critical velocity ($w_{r,SS} < -w_{C,SS}$) are able to get close. By balancing the Coulomb energy barrier and the relative kinetic energy, the critical velocity can be given as

$$w_{C,SS} = \left(\frac{q^2}{2\pi\epsilon_0 r m_{SS}}\right)^{1/2}. \quad (3.8)$$

The critical velocity for LL or SL pairs can be given by replacing $m_{SS} = m_S/2$ with $m_{LL} = m_L/2$ or $m_{SL} = m_S m_L / (m_S + m_L)$. Note that the critical velocity is derived from the interaction between a pair of particles, which could reasonably describe the major effect of the Coulomb force in the current dilution suspension. If the particle concentration becomes higher, the particle number density needs to be included for a more accurate prediction (Boutsikakis *et al.* 2022, 2023). By assuming a sharp cutoff at $w = -w_{C,SS}$, Lu & Shaw (2015) related the RDF of charged SS pairs $g_{SS}(r|q)$ to that of neutral SS pairs

$g_{SS}(r|q = 0)$ as

$$g_{SS}(r|q) = g_{SS}(r|q = 0) \cdot \frac{\int_{-\infty}^{-w_{C,SS}} p_{r,SS}(w) dw}{\int_{-\infty}^0 p_{r,SS}(w) dw} = g_{r,SS}(r|q = 0) \cdot \left[1 - \operatorname{erf}\left(\frac{w_{C,SS}}{\sqrt{2}\sigma_{SS}}\right) \right], \tag{3.9}$$

where erf is the error function. However, as the relative velocity magnitude w_r becomes smaller than $w_{C,SS}$, the corresponding flux contribution does not drop sharply to zero. Instead, a smooth transition would be expected, so the ratio of the charged RDF to the neutral RDF should be written as

$$\frac{g_{SS}(r|q)}{g_{SS}(r|q = 0)} = \frac{\int_{-\infty}^0 \Theta_{SS}(w)p_{r,SS}(w) dw}{\int_{-\infty}^0 p_{r,SS}(w) dw}. \tag{3.10}$$

Here, $\Theta_{SS}(w)$ is the electrical kernel that gradually transitions from one to zero when the magnitude of w_r drops below $w_{C,SS}$. The proportion of charged particles that could overcome the Coulomb repulsion is then obtained from the convolution of Θ_{SS} and $p_{r,SS}$, which is the numerator of the right-hand term in (3.10). To account for the smooth transition without adding significant complexity, we still adopt the sharp cutoff assumption, but the effective cutoff velocity $\beta_{SS}w_{C,SS}$ is used. Here, $\beta_{SS} \sim O(1)$ is the correction factor that ensures an accurate prediction as

$$\int_{-\infty}^0 \Theta_{SS}(w)p_{r,SS}(w) dw \approx \int_{-\infty}^{-\beta_{SS}w_{C,SS}} p_{r,SS}(w) dw. \tag{3.11}$$

The difference between the effective cutoff and the actual electrical kernel will be further discussed in § 3.3. Consequently, (3.9) becomes

$$g_{SS}(r|q) = g_{SS}(r|q = 0) \cdot \left[1 - \operatorname{erf}\left(\frac{\beta_{SS} \cdot w_{C,SS}}{\sqrt{2}\sigma_{SS}}\right) \right]. \tag{3.12}$$

To obtain the mean relative velocity between charged SS pairs, we start by computing the mean relative velocity in the velocity interval $[-\infty, -\beta_{SS}w_{C,SS}]$ between neutral SS pairs

$$\begin{aligned} \langle |w'_{r,SS}| \rangle(r|q = 0) &= \frac{-\int_{-\infty}^{-\beta_{SS}w_{C,SS}} w \cdot p_{r,SS}(w) dw}{\int_{-\infty}^{-\beta_{SS}w_{C,SS}} p_{r,SS}(w) dw} \\ &= \langle |w_{r,SS}| \rangle(r|q = 0) \cdot \exp\left(\frac{-\beta_{SS}^2 w_{C,SS}^2}{2\sigma_{SS}^2}\right) / \left[1 - \operatorname{erf}\left(\frac{\beta_{SS} \cdot w_{C,SS}}{\sqrt{2}\sigma_{SS}}\right) \right]. \end{aligned} \tag{3.13}$$

Then, the mean relative velocity of charged SS pairs can be obtained by subtracting the Coulomb potential energy from the mean relative kinetic energy in the velocity

interval $[-\infty, -\beta_{SS}w_{C,SS}]$

$$\frac{1}{2}m_{SS}\langle |w_{r,SS}|^2(r|q) \rangle = \frac{1}{2}m_{SS}\langle |w'_{r,SS}|^2(r|q=0) \rangle - \frac{\beta_{SS}^2q^2}{4\pi\epsilon_0r}. \quad (3.14)$$

Here, the correction factor β_{SS} is also added to the last term on the right-hand side to account for the smooth transition. Taking (3.13) into (3.14) then yields

$$\langle |w_{r,SS}| \rangle(r|q) = \langle |w_{r,SS}| \rangle(r|q=0) \cdot \left[\frac{\exp\left(-\frac{\beta_{SS}^2w_{C,SS}^2}{\sigma_{SS}^2}\right)}{\left[1 - \operatorname{erf}\left(\frac{\beta_{SS}w_{C,SS}}{\sqrt{2}\sigma_{SS}}\right)\right]^2} - \frac{\beta_{SS}^2q^2}{2\pi\epsilon_0m_{SS} \cdot \langle |w_{r,SS}|^2(r|q=0) \rangle \cdot r} \right]^{1/2}. \quad (3.15)$$

Finally, by multiplying (3.9) and (3.15) and taking into account the definition of Ct_0 (3.6), the flux ratio can be given as

$$\begin{aligned} \frac{\Phi_{SS}(q)}{\Phi_{SS}(q=0)} &= \frac{g_{SS}(r|q) \cdot \langle |w_{r,SS}| \rangle(r|q)}{g_{SS}(r|q=0) \cdot \langle |w_{r,SS}| \rangle(r|q=0)} \\ &= \left\{ \exp\left(-\frac{2\beta_{SS}^2Ct_0}{\pi}\right) - \beta_{SS}^2Ct_0[1 - \operatorname{erf}(\beta_{SS}\sqrt{Ct_0/\pi})]^2 \right\}^{1/2}. \end{aligned} \quad (3.16)$$

The flux ratios for LL pairs and SL pairs can be derived in a similar way and are written as

$$\frac{\Phi_{LL}(q)}{\Phi_{LL}(q=0)} = \left\{ \exp\left(-\frac{2\beta_{LL}^2Ct_0}{\pi}\right) - \beta_{LL}^2Ct_0[1 - \operatorname{erf}(\beta_{LL}\sqrt{Ct_0/\pi})]^2 \right\}^{1/2}, \quad (3.17a)$$

$$\frac{\Phi_{SL}(q)}{\Phi_{SL}(q=0)} = \left\{ \exp\left(-\frac{2\beta_{SL}^2Ct_0}{\pi}\right) + \beta_{SL}^2Ct_0[1 + \operatorname{erf}(\beta_{SL}\sqrt{Ct_0/\pi})]^2 \right\}^{1/2}. \quad (3.17b)$$

Equations (3.16) and (3.17) are then fitted as blue lines in figure 5, which show good agreement with the simulation results. The fitted correction factors are $\beta_{SS} = 0.193$, $\beta_{LL} = 0.739$ and $\beta_{SL} = 0.5415$, satisfying the assumption that the correction factors are of the order of unity. The predictions with the fixed $\beta = 1$ are also shown as brown dash-dotted lines, which correspond to the original model that assumes the sharp cutoff occurs at the critical velocity $w_{C,SS/LL/SL}$. Although the trends are similar, models with the fixed $\beta = 1$ underestimate the critical Ct_0 at which the transition occurs. Moreover, the proposed model underestimates the SS flux when $Ct_0 \approx 10^2$ in figure 5(a). To find the origin of this discrepancy, the predicted $g_{ij}(r)$ using (3.12) and the predicted $\langle |w_{r,SS}| \rangle(r)$ using (3.15) are also plotted as grey dashed lines in figures 2 and 3, respectively. It can be seen that the predicted RDFs are comparable to the simulation results, so the discrepancy of Φ_{SS} at $Ct_0 \approx 10^2$ mainly comes from the underestimation of the mean relative velocity at $r \sim \eta$ in figure 3(a). Since the PDF of w_r is assumed Gaussian in our model, the influence of intermittency is not considered. As a result, the proportion of particle pairs with large relative velocity is significantly underestimated.

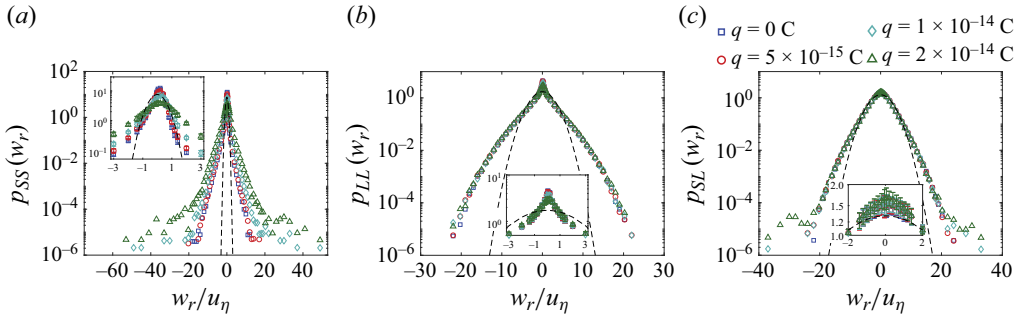


Figure 6. The PDFs of the relative velocity between (a) SS, (b) LL and (c) SL pairs at $r \in [1.15\eta, 2.5\eta]$. Zoom-in views around $w_r = 0$ are shown in the insets. Black dashed lines denote the Gaussian distributions defined by (3.7) for different kinds of particle pairs.

3.3. Particle flux density for charged particles

In § 3.2, the mean Coulomb-turbulence parameter Ct_0 is defined using the mean relative velocity $\langle |w_{r,ij}| \rangle$, which compares the importance of the Coulomb force with the mean relative motion caused by turbulence. However, it has been known that the relative velocity between particle pairs may vary within a wide range, and the mean Coulomb-turbulence parameter Ct_0 may not be sufficient to fully reveal the physics.

In this section it would be of interest to examine the impacts of the Coulomb force on particle pairs with different relative velocities. For different kinds of particle pairs, the particle flux Φ_{ij} in the relative velocity space is expanded as

$$\Phi_{ij} = \int_{-\infty}^{\infty} \phi_{ij}(w_r) dw_r. \tag{3.18}$$

Here, ϕ_{ij} is the density of particle flux within each relative velocity interval, which measures the contribution to the total particle flux Φ_{ij} by particle pairs whose relative velocity is within the interval $w_r \pm \Delta w_r/2$. By comparing (3.18) and (3.3), ϕ_{ij} can be given as

$$\phi_{ij} = \frac{1}{2} g_{ij} \cdot |w_{r,ij}| p_{ij}(w_{r,ij}). \tag{3.19}$$

We start with the effect of the Coulomb force on the PDFs of relative velocity $p_{ij}(w_{r,ij})$, because the distribution of ϕ_{ij} in (3.19) is strongly dependent on $p_{ij}(w_{r,ij})$. Figure 6(a) illustrates PDFs of $w_{r,SS}$ at the separation distance interval $r \in [1.15\eta, 2.5\eta]$. The Gaussian distribution defined by (3.7) is also shown as the black dashed line. By comparing the neutral PDFs and the Gaussian curves, it is clear that the Gaussian assumption serves as a reasonable approximation at $|w_r| < 3u_\eta$, but significantly underestimates the probability of large $|w_r|$. Therefore, the Gaussian assumption is only suitable for modelling low-order effects, not for higher-order statistics. Besides, as will be discussed below, since the Gaussian curve is symmetric, it is not able to capture the asymmetry of the relative velocity between approaching and departing pairs.

For SS pairs, compared with the neutral PDF, charged PDFs become wider as q increases, indicating a lower/higher probability of finding particle pairs with low/high relative velocity within the separation interval. This is consistent with the increase of the mean relative velocity with q in figure 3(a). If we look at the symmetry of p_{SS} , the neutral PDF is found negatively skewed. This asymmetry is attributed to: (i) the fluid velocity derivative is negatively skewed, and the relative motion between particle pairs

$q(\times 10^{-14} \text{ C})$	$\langle w_{r,SS}^3 \rangle / [\langle w_{r,SS}^2 \rangle]^{3/2}$	$\langle w_{r,LL}^3 \rangle / [\langle w_{r,LL}^2 \rangle]^{3/2}$	$\langle w_{r,SL}^3 \rangle / [\langle w_{r,SL}^2 \rangle]^{3/2}$
0	-2.144	-0.074	-0.081
0.5	-1.817	-0.079	-0.093
1	-1.066	-0.073	-0.089
2	-0.500	-0.075	-0.114

Table 2. Normalized skewness of the radial relative velocity w_r at $r \in [1.15\eta, 2.5\eta]$.

with $St = 1$ is partially coupled to the local flow and thus exhibits a similar feature (Van Atta & Antonia 1980; Wang *et al.* 2000); (ii) the asymmetry of particle path history gives rise to a larger relative velocity between approaching pairs than departing pairs (Bragg & Collins 2014). However, the asymmetry of p_{SS} curves are significantly reduced once particles are charged (see table 2), which results from the symmetric nature of the Coulomb force. The magnitude of the Coulomb force relies only on the interparticle distance r , so the approaching or departing SS pairs experience the same amount of repulsion as long as r is the same, which makes the approaching-then-departing process more symmetric. Therefore, introducing Coulomb force could effectively increase the standard deviation but reduce the skewness of $w_{r,SS}$.

For LL pairs, since Coulomb repulsion is only able to repel pairs with small relative velocity, p_{LL} drops slightly as w_r approaches zero, but remains almost unchanged at larger w_r . As for p_{SL} , the difference between the neutral and charged case is insignificant, which again demonstrates that the velocity difference between particles of different sizes mainly comes from the differential inertia effect, while the influence of the Coulomb force is limited. Besides, the movement of large particles with $St = 10$ has very weak couplings to the local flow fields, so the skewness of p_{LL} and p_{SL} in table 2 is negligible.

We now turn to the distribution of flux density ϕ_{ij} in the velocity space. Figure 7(a,c,e) plots the flux densities between SS, LL and SL pairs, respectively. Different from the unimodal PDFs of the relative velocity shown in figure 6, ϕ_{ij} are bimodal because the maximum flux density is reached when the product $|w_{r,ij}| \cdot p_{ij}(w_{r,ij})$ is the largest. Therefore, it is the particle pairs with the intermediate relative velocity that contribute the most to the overall particle flux.

To better describe the impacts of the Coulomb force, we define the Coulomb kernel Θ_{ij} as the ratios of the charged flux densities to their neutral values, i.e. $\Theta_{ij}(q) = \phi_{ij}(q) / \phi_{ij}(q = 0)$, which are displayed in the right panel (i.e. (b), (d) and (f)) of figure 7. As shown in figure 7(b), the value of Θ_{SS} varies by more than one order of magnitude, indicating that the influence of the Coulomb force changes significantly as w_r changes. When $|w_r|$ is small, Θ_{SS} decreases drastically as q increases because Coulomb repulsion dominates. In addition, Θ_{SS} is found to be asymmetric. As discussed above, neutral particles with $St = 1$ tend to separate at a lower relative velocity compared with the approaching pairs. When they are charged, particle pairs originally separating at low speeds will be accelerated and pushed apart by Coulomb repulsion, which effectively shifts the high flux density from the small positive w_r to a larger positive w_r in the velocity space. Consequently, Θ_{SS} experiences a more significant decrease at w_r slightly greater than zero, but quickly exceeds one when $w_r \approx 2u_\eta$. Moreover, Θ_{SS} becomes larger than one at large $|w_r|$ for both approaching and departing pairs. The explanation is that, with the increase of q , small particles are more likely to get attracted towards the large ones and follow their motions. Since the relative velocity between LL pairs is generally much larger, this

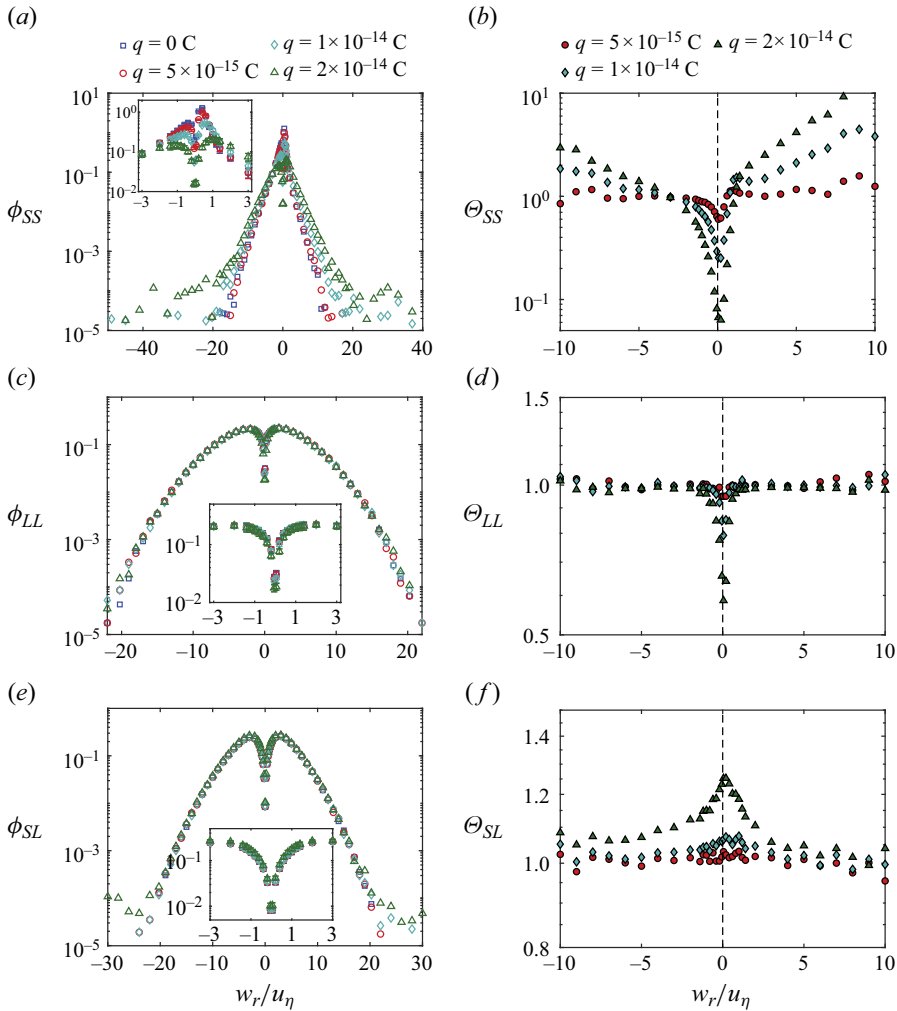


Figure 7. Particle flux density in the velocity space, $\phi(w_r)$, between (a) SS, (c) LL and (e) SL pairs at $r \in [1.15\eta, 2.5\eta]$. Zoom-in views around $w_r = 0$ are shown in the insets. (b,d,f) Dependence of Coulomb kernel $\Theta_{ij} = \phi_{ij}(q)/\phi_{ij}(q = 0)$ on $w_{r,ij}$ corresponding to (a,c,e), respectively.

effect could increase the SS flux density at large $|w_r|$. However, the contribution of the increased flux at large positive $|w_r|$ is negligible compared with the decrease at small $|w_r|$ (see figure 7a), so the major effect of the Coulomb force is to reduce the SS flux through the SS repulsive force.

The kernel Θ_{LL} between LL pairs (figure 7d) also drops quickly at small $|w_r|$, but recovers to unity when $|w_r| \geq 2u_\eta$. Besides, because of the limited effects of the local fluid velocity gradient mentioned above, the approaching and departing processes are more symmetric for neutral LL pairs, and adding the Coulomb force retains this symmetry. As for Θ_{SL} shown in figure 7(f), the change is still most significant near $w_r = 0$. However, different from the kernels of SS/LL pairs where the impact of the same-sign repulsion is only obvious within a narrow interval (i.e. $|w_r|/u_\eta \leq 2$), the opposite-sign attraction seems to increase Θ_{SL} in a much wider range of w_r . For instance, Θ_{SL} is increased even at $w_r/u_\eta = -10$ for $q = 2 \times 10^{-14}$ C in figure 7(f). As discussed in § 3.2, the main effect of

the opposite-sign attraction is to enhance SL clustering. Then, particles of different sizes, although staying close to each other, will develop a large relative velocity as a result of their different responses to local fluctuations, which leads to the increase of Θ_{SL} in a wide range of w_r .

The discussion above has shown that the influence of the Coulomb force is different as the particle relative velocity $w_{r,ij}$ changes. Therefore, instead of using the mean relative velocity $\langle |w_{r,ij}| \rangle$ (3.6), we adopt the median relative velocity $\bar{w}_{r,ij}$ in each w_r bin to estimate the relative kinetic energy. For a given separation distance r and a certain relative velocity bin with the median $\bar{w}_{r,ij}$, the extended Coulomb-turbulence parameter is given as

$$Ct \equiv \frac{q_i q_j}{2\pi\epsilon_0 r m_{ij} \bar{w}_{r,ij}^2}. \quad (3.20)$$

We then examine the dependence of the electrical kernel Θ_{ij} on the extended Coulomb-turbulence parameter Ct . For the data points $(w_{r,ij}, \Theta_{ij})$ shown in the right panel (i.e. (b), (d) and (f)) of figure 7, the corresponding values of Ct are calculated using (3.20), and the results are re-plotted as points (Ct, Θ_{ij}) . Note that to ensure meaningful statistics, only data points satisfying a certain criterion are considered and the reasons are as follows:

- (i) In addition to the separation interval $r \in [1.15\eta, 2.5\eta)$ shown in figure 7, data from two more separation intervals, i.e. $[0.85\eta, 1.15\eta)$ and $[2.5\eta, 3.5\eta)$, are also added. At these separation distances, the effect of the electrostatic force is already significant, while the number of samples is large enough for statistics.
- (ii) We only consider pairs with their relative velocity in a certain range to avoid using the more scattered data points at large w_r . For SS pairs, the relative velocity range is $[-5u_\eta, 5u_\eta]$, while for LL/SL pairs the range considered is $[-10u_\eta, 10u_\eta]$. The particle flux within the above ranges contributes at least 97.1%/95.6%/96.3% of the total SS/LL/SL particle flux in the neutral case, which reflects the major change of Φ_{ij} in each case.
- (iii) As shown in figure 7(b), Θ_{SS} is not symmetric about $w_r = 0$. When particles are departing, the Coulomb repulsion will redistribute ϕ_{SS} in the velocity space, which may distort the $\Theta_{SS} - Ct$ relationship. We therefore only use the data from approaching pairs ($w_r < 0$) for later analysis. Since the outward flux is balanced by the inward flux in the steady state, the total flux could still be evaluated as $\Phi_{SS}(q) = 2 \int_{-\infty}^0 \Theta_{SS}(Ct) \phi_{SS}(w_{r,SS}) dw_{r,SS}$.

Figure 8 plots the dependence of Θ_{ij} on Ct for different particle pairs. Despite different particle charge q and separation r , the data points for both SS (figure 8a) and LL (figure 8b) pairs show a similar trend. When Ct is small, the Coulomb force is weak compared with particle-turbulence interaction, so Θ_{SS} and Θ_{LL} stay close to one. When Ct becomes larger than one, the same-sign repulsion starts to significantly reduce the corresponding particle flux density, and a decrease of Θ is observed. In § 3.2, it has been assumed that a sharp cutoff occurs at the effective velocity $\beta_{SS} w_{C,SS}$ or $\beta_{LL} w_{C,LL}$ for SS or LL pairs. However, the transitions of Θ_{SS} and Θ_{LL} in figure 8(a) turn out to be smooth. Thus, the sharp cutoff can be understood as the first-order approximation of the influence of Coulomb repulsion, which can be written as

$$\Theta_{ij}(Ct) = 1 - H(Ct_{crit,ij}), \quad (3.21)$$

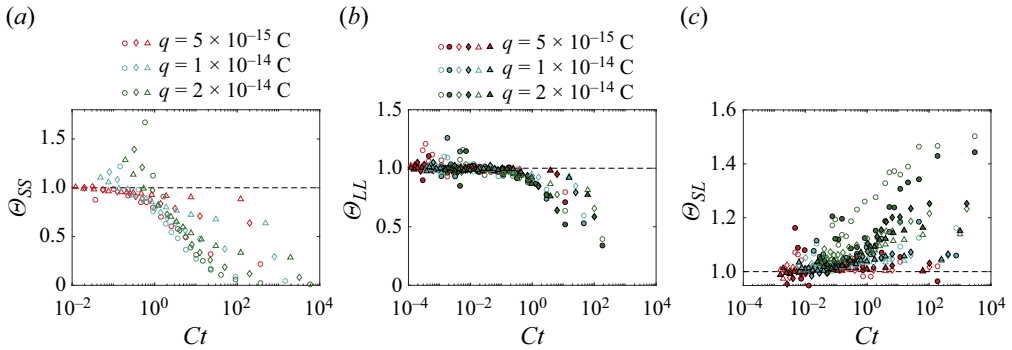


Figure 8. Dependence of the electrical kernel Θ_{ij} on the extended Coulomb-turbulence parameter Ct for (a) SS, (b) LL and (c) SL particle pairs. Different shapes represent data points from $r \in [0.85\eta, 1.15\eta)$ (circles: \circ), $r \in [1.15\eta, 2.5\eta)$ (diamonds: \diamond) and $r \in [2.5\eta, 3.5\eta)$ (triangles: Δ), respectively. Open/filled symbols denote data points for approaching/departing pairs.

with $H(\cdot)$ being the Heaviside step function. The critical value of Ct describing where Θ_{ij} steps down can be related to the fitted correction factors for the effective cutoff velocity as

$$Ct_{crit,ij} = 1/\beta_{ij}^2. \quad (3.22)$$

By taking into the fitted results ($\beta_{SS} = 0.193$ and $\beta_{LL} = 0.739$) from § 3.2, the critical values can be given as $Ct_{crit,SS} = 26.85$ and $Ct_{crit,LL} = 1.83$, respectively.

However, different from Θ_{SS} and Θ_{LL} , there is no clear dependence of Θ_{SL} on Ct in figure 8(c). The reason is as follows. The opposite-sign Coulomb force will attract SL pairs with a low departing velocity together and promote clustering. However, although these SL pairs have a low relative velocity at first, they will develop a much larger relative velocity over time. As a result, the relative kinetic energy E_{Kin} becomes independent of the electrical potential energy E_{Coul} , and no clear relationship can be found between Θ_{SL} and ϕ_{SL} .

4. Conclusions

In this study, we investigate the effects of charge segregation on the dynamics of tribocharged bidispersed particles in homogeneous isotropic turbulence by means of DNS. Using a radial distribution function $g_{ij}(r)$, we show that Coulomb repulsion/attraction significantly inhibits/promotes particle clustering within a short range, while the clustering at a large separation distance is still determined by particle–turbulence interaction. For same-sign particles, Coulomb repulsion repels an approaching pair with low relative velocity, giving rise to the increase of mean relative velocity $\langle |w_{r,ij}| \rangle$ as the separation distance r decreases. In comparison, the relative velocity between different-size particles is almost unchanged for all q , which suggests that the differential inertia effect contributes predominantly to $\langle w_{r,SL} \rangle$.

By defining the particle flux Φ_{ij} as the number of particles crossing the collision sphere per area per unit time, we are able to quantify the particle collision frequency without a prescribed collision diameter R_C . As expected, the Coulomb repulsion/attraction is found to reduce/increase the total particle flux Φ_{ij} when particles are close. When plotted as a function of the mean Coulomb-turbulence parameter Ct_0 that measures the relative importance of electrostatic potential energy to the mean relative kinetic energy, the particle flux ratio $\Phi_{ij}(q)/\Phi_{ij}(q=0)$ is shown to follow a similar trend. Specifically, by assuming

that the PDF of relative velocity follows a Gaussian distribution, the particle flux can be well modelled by a function of Ct_0 .

The total particle flux Φ_{ij} is then expanded in the relative velocity space as the flux density ϕ_{ij} , and the relative change $\Theta_{ij} = \phi_{ij}(q)/\phi_{ij}(q=0)$ (also termed the Coulomb kernel) in each relative interval exhibits a significant difference. Finally, the extended Coulomb-turbulence parameter Ct is defined using the median $\bar{w}_{r,ij}$ in each relative velocity bin, which better describes the competition between Coulomb force and the turbulence effect. Then for same-size particle pairs, a clear relationship is found between Θ_{ij} and Ct . And the smooth transition of Θ_{ij} is observed near the critical value $Ct_{crit,ij} = 1/\beta_{ij}^2$. For SL pairs, however, the relative velocity will grow larger because of the predominant differential inertia effect, so Θ_{SL} shows no clear dependence on $w_{r,SL}$ (and therefore on Ct).

Funding. This work was supported by an Early Stage Innovation grant from NASA’s Space Technology Research Grants Program under grant no. 80NSSC21K0222. This work was also partially supported by the Office of Naval Research (ONR) under grant no. N00014-21-1-2620.

Declaration of interests. The authors report no conflict of interest.

Author ORCIDs.

 Xuan Ruan <https://orcid.org/0000-0002-7890-5390>;

 Rui Ni <https://orcid.org/0000-0002-7178-1479>.

Appendix A. Validation of the electrostatic calculation

To validate the electrostatic computation introduced in § 2.3, we compute the Coulomb force acting on N_p particles in the three-dimensional periodic box using both (i) FMM incorporated with periodic image boxes and (ii) the standard Ewald summation. For the charge-neutral system in this work, the exact Coulomb force acting on particle i can be computed by Ewald summation (Deserno & Holm 1998) as

$$\mathbf{F}_i^{E,Ewald} = \mathbf{F}_i^{(r)} + \mathbf{F}_i^{(k)} + \mathbf{F}_i^{(d)}, \tag{A1}$$

where the contributions from the real (physical) space $\mathbf{F}_i^{(r)}$, the Fourier (wavenumber) space $\mathbf{F}_i^{(k)}$ and the dipole correction $\mathbf{F}_i^{(d)}$ are given as

$$\mathbf{F}_i^{(r)} = \frac{q_i}{4\pi\epsilon_0} \sum_j q_j \sum_{\mathbf{m} \in \mathbb{Z}^3} \left(\frac{2\alpha}{\sqrt{\pi}} \exp(-\alpha^2 |\mathbf{r}_{ij} + \mathbf{m}L|^2) + \frac{\text{erfc}(\alpha |\mathbf{r}_{ij} + \mathbf{m}L|)}{|\mathbf{r}_{ij} + \mathbf{m}L|} \right) \frac{\mathbf{r}_{ij} + \mathbf{m}L}{|\mathbf{r}_{ij} + \mathbf{m}L|^2}, \tag{A2a}$$

$$\mathbf{F}_i^{(k)} = \frac{q_i}{4\pi\epsilon_0 L^3} \sum_j q_j \sum_{\mathbf{k} \neq \mathbf{0}} \frac{4\pi\mathbf{k}}{k^2} \exp\left(-\frac{k^2}{4\alpha^2}\right) \sin(\mathbf{k} \cdot \mathbf{r}_{ij}), \tag{A2b}$$

$$\mathbf{F}_i^{(d)} = -\frac{q_i}{\epsilon_0(1 + 2\epsilon')L^3} \sum_j q_j \mathbf{x}_j. \tag{A2c}$$

Here, α is the Ewald parameter, erfc is the complimentary error function and $\epsilon' = 1$ is the relative dielectric constant of the surrounding medium.

Since Ewald summation is computationally expensive, a smaller-scale system with $N_p = 2000$ oppositely charged particles is used in validation cases. In each case, ten parallel computations with different particle locations are performed to ensure reliable

Parameters	Symbols	Values
Domain size	L	2π
Particle number	N_p	2000
Particle charge	q	± 1
Accuracy parameter	αr_C	π
Cutoff distance in real space	r_C	π
Cutoff wavenumber in Fourier space	k_C	6
Error in real space	$\epsilon^{(r)}$	1.65×10^{-5}
Error in Fourier space	$\epsilon^{(k)}$	2.06×10^{-5}

Table 3. Dimensionless parameters in Ewald summation.

N_{per}	0	1	2	3	4
ϵ^{FMM}	1.12×10^{-1}	2.13×10^{-3}	1.70×10^{-3}	1.65×10^{-3}	1.63×10^{-3}

Table 4. Relative errors of FMM computation compared with Ewald summation.

statistics. Table 3 lists parameters used in the Ewald summation. The dimensionless product αr_C equals π to ensure high accuracy in both real and Fourier spaces. The cutoff radius(r_C)/wavenumber(k_C) in the real/Fourier space is then determined by $r_C = (\alpha r_C)L/\pi^{1/2}N_p^{1/6}$ and $k_C = 1.8(\alpha r_C)^2/r_C$ to balance the computation cost of $F_i^{(r)}$ and $F_i^{(k)}$ (Fincham 1994).

When performing FMM computation, the layer number N_{per} is varied from 0 to 4 to show the influence of adding image domains. The relative error of FMM compared with Ewald summation is given as

$$\epsilon^{FMM} = \frac{|\mathbf{F}^{E,FMM} - \mathbf{F}^{E,Ewald}|}{|\mathbf{F}^{E,Ewald}|} = \frac{\left[\sum_{i=1}^{N_p} (\mathbf{F}_i^{E,FMM} - \mathbf{F}_i^{E,Ewald})^2 / N_p \right]^{1/2}}{\left[\sum_{i=1}^{N_p} (\mathbf{F}_i^{E,Ewald})^2 / N_p \right]^{1/2}}, \quad (A3)$$

where the norm of force is defined as the root mean square of the force components following Deserno & Holm (1998). The dependence of ϵ^{FMM} on N_{per} is shown in table 4. The relative error is significant ($\epsilon^{FMM} > 10\%$) if periodicity is not considered. After adding image domains, the relative error drops significantly and almost saturates after $N_{per} \geq 2$. Hence, $N_{per} = 2$ is chosen to guarantee sufficient accuracy ($\epsilon^{FMM} = 0.17\%$) while avoiding expensive computation cost.

REFERENCES

- ABABAEI, A., ROSA, B., POZORSKI, J. & WANG, L.-P. 2021 On the effect of lubrication forces on the collision statistics of cloud droplets in homogeneous isotropic turbulence. *J. Fluid Mech.* **918**, A22.
- ARGUEDAS-LEIVA, J.-A., SŁOMKA, J., LALESCU, C.C., STOCKER, R. & WILCZEK, M. 2022 Elongation enhances encounter rates between phytoplankton in turbulence. *Proc. Natl Acad. Sci. USA* **119** (32), e2203191119.

Charged bidispersed particles in turbulence

- AYALA, O., ROSA, B. & WANG, L.-P. 2008a Effects of turbulence on the geometric collision rate of sedimenting droplets. Part 2. Theory and parameterization. *New J. Phys.* **10** (7), 075016.
- AYALA, O., ROSA, B., WANG, L.-P. & GRABOWSKI, W.W. 2008b Effects of turbulence on the geometric collision rate of sedimenting droplets. Part 1. Results from direct numerical simulation. *New J. Phys.* **10** (7), 075015.
- BAKER, L., FRANKEL, A., MANI, A. & COLETTI, F. 2017 Coherent clusters of inertial particles in homogeneous turbulence. *J. Fluid Mech.* **833**, 364–398.
- BALACHANDAR, S. & EATON, J.K. 2010 Turbulent dispersed multiphase flow. *Annu. Rev. Fluid Mech.* **42**, 111–133.
- BALKOVSKY, E., FALKOVICH, G. & FOUXON, A. 2001 Intermittent distribution of inertial particles in turbulent flows. *Phys. Rev. Lett.* **86** (13), 2790.
- BEC, J., BIFERALE, L., CENCINI, M., LANOTTE, A., MUSACCHIO, S. & TOSCHI, F. 2007 Heavy particle concentration in turbulence at dissipative and inertial scales. *Phys. Rev. Lett.* **98** (8), 084502.
- BEC, J., BIFERALE, L., CENCINI, M., LANOTTE, A.S. & TOSCHI, F. 2011 Spatial and velocity statistics of inertial particles in turbulent flows. *J. Phys.: Conf. Ser.* **333**, 012003.
- BEWLEY, G.P., SAW, E.-W. & BODENSCHATZ, E. 2013 Observation of the sling effect. *New J. Phys.* **15** (8), 083051.
- BOUTSIKAKIS, A., FEDE, P. & SIMONIN, O. 2022 Effect of electrostatic forces on the dispersion of like-charged solid particles transported by homogeneous isotropic turbulence. *J. Fluid Mech.* **938**, A33.
- BOUTSIKAKIS, A., FEDE, P. & SIMONIN, O. 2023 Quasi-periodic boundary conditions for hierarchical algorithms used for the calculation of inter-particle electrostatic interactions. *J. Comput. Phys.* **472**, 111686.
- BRAGG, A.D. & COLLINS, L.R. 2014 New insights from comparing statistical theories for inertial particles in turbulence. II. Relative velocities. *New J. Phys.* **16** (5), 055014.
- BRAGG, A.D., HAMMOND, A.L., DHARIWAL, R. & MENG, H. 2022 Hydrodynamic interactions and extreme particle clustering in turbulence. *J. Fluid Mech.* **933**, A31.
- CALZAVARINI, E., CENCINI, M., LOHSE, D. & TOSCHI, F. 2008 Quantifying turbulence-induced segregation of inertial particles. *Phys. Rev. Lett.* **101** (8), 084504.
- CHUN, J., KOCH, D.L., RANI, S.L., AHLUWALIA, A. & COLLINS, L.R. 2005 Clustering of aerosol particles in isotropic turbulence. *J. Fluid Mech.* **536**, 219–251.
- DESERNO, M. & HOLM, C. 1998 How to mesh up ewald sums. I. A theoretical and numerical comparison of various particle mesh routines. *J. Chem. Phys.* **109** (18), 7678–7693.
- DI RENZO, M. & URZAY, J. 2018 Aerodynamic generation of electric fields in turbulence laden with charged inertial particles. *Nat. Commun.* **9**, 1676.
- FALKOVICH, G., FOUXON, A. & STEPANOV, M.G. 2002 Acceleration of rain initiation by cloud turbulence. *Nature* **419** (6903), 151–154.
- FALKOVICH, G., GAWEDZKI, K. & VERGASSOLA, M. 2001 Particles and fields in fluid turbulence. *Rev. Mod. Phys.* **73** (4), 913.
- FALKOVICH, G. & PUMIR, A. 2007 Sling effect in collisions of water droplets in turbulent clouds. *J. Atmos. Sci.* **64** (12), 4497–4505.
- FINCHAM, D. 1994 Optimisation of the ewald sum for large systems. *Mol. Simul.* **13** (1), 1–9.
- FORWARD, K.M., LACKS, D.J. & SANKARAN, R.M. 2009 Charge segregation depends on particle size in triboelectrically charged granular materials. *Phys. Rev. Lett.* **102** (2), 028001.
- GIMBUTAS, Z. & GREENGARD, L. 2015 Computational software: simple FMM libraries for electrostatics, slow viscous flow, and frequency-domain wave propagation. *Commun. Comput. Phys.* **18** (2), 516–528.
- GOTO, S. & VASSILICOS, J.C. 2006 Self-similar clustering of inertial particles and zero-acceleration points in fully developed two-dimensional turbulence. *Phys. Fluids* **18** (11), 115103.
- GOTO, S. & VASSILICOS, J.C. 2008 Sweep-stick mechanism of heavy particle clustering in fluid turbulence. *Phys. Rev. Lett.* **100** (5), 054503.
- GRABOWSKI, W.W. & WANG, L.-P. 2013 Growth of cloud droplets in a turbulent environment. *Annu. Rev. Fluid Mech.* **45**, 293–324.
- GREENGARD, L. & ROKHLIN, V. 1987 A fast algorithm for particle simulations. *J. Comput. Phys.* **73** (2), 325–348.
- GREENGARD, L. & ROKHLIN, V. 1997 A new version of the fast multipole method for the laplace equation in three dimensions. *Acta Numerica* **6**, 229–269.
- GUSTAVSSON, K. & MEHLIG, B. 2014 Relative velocities of inertial particles in turbulent aerosols. *J. Turbul.* **15** (1), 34–69.
- HARPER, J.M., CIMARELLI, C., CIGALA, V., KUEPPERS, U. & DUFEK, J. 2021 Charge injection into the atmosphere by explosive volcanic eruptions through triboelectrification and fragmentation charging. *Earth Planet. Sci. Lett.* **574**, 117162.

- HARRISON, R.G., NICOLL, K.A., AMBAUM, M.H.P., MARLTON, G.J., APLIN, K.L. & LOCKWOOD, M. 2020 Precipitation modification by ionization. *Phys. Rev. Lett.* **124** (19), 198701.
- IRELAND, P.J., BRAGG, A.D. & COLLINS, L.R. 2016a The effect of reynolds number on inertial particle dynamics in isotropic turbulence. Part 1. Simulations without gravitational effects. *J. Fluid Mech.* **796**, 617–658.
- IRELAND, P.J., BRAGG, A.D. & COLLINS, L.R. 2016b The effect of reynolds number on inertial particle dynamics in isotropic turbulence. Part 2. Simulations with gravitational effects. *J. Fluid Mech.* **796**, 659–711.
- JAWOREK, A., MARCHEWICZ, A., SOBCZYK, A.T., KRUPA, A. & CZECH, T. 2018 Two-stage electrostatic precipitators for the reduction of ± 2.5 Particle emission. *Prog. Energy Combust. Sci.* **67**, 206–233.
- KARNIK, A.U. & SHRIMPTON, J.S. 2012 Mitigation of preferential concentration of small inertial particles in stationary isotropic turbulence using electrical and gravitational body forces. *Phys. Fluids* **24** (7), 073301.
- LEE, V., WAITUKAITIS, S.R., MISKIN, M.Z. & JAEGER, H.M. 2015 Direct observation of particle interactions and clustering in charged granular streams. *Nat. Phys.* **11** (9), 733–737.
- LIU, Y., SHEN, L., ZAMANSKY, R. & COLETTI, F. 2020 Life and death of inertial particle clusters in turbulence. *J. Fluid Mech.* **902**, R1.
- LU, J., NORDSIEK, H., SAW, E.W. & SHAW, R.A. 2010a Clustering of charged inertial particles in turbulence. *Phys. Rev. Lett.* **104** (18), 184505.
- LU, J., NORDSIEK, H. & SHAW, R.A. 2010b Clustering of settling charged particles in turbulence: theory and experiments. *New J. Phys.* **12** (12), 123030.
- LU, J. & SHAW, R.A. 2015 Charged particle dynamics in turbulence: theory and direct numerical simulations. *Phys. Fluids* **27** (6), 065111.
- MARSHALL, J.S. 2009 Discrete-element modeling of particulate aerosol flows. *J. Comput. Phys.* **228** (5), 1541–1561.
- MARSHALL, J.S. & LI, S. 2014 *Adhesive Particle Flow*. Cambridge University Press.
- MATHAI, V., CALZAVARINI, E., BRONS, J., SUN, C. & LOHSE, D. 2016 Microbubbles and microparticles are not faithful tracers of turbulent acceleration. *Phys. Rev. Lett.* **117** (2), 024501.
- MAXEY, M.R. 1987 The gravitational settling of aerosol particles in homogeneous turbulence and random flow fields. *J. Fluid Mech.* **174**, 441–465.
- MAXEY, M.R. & RILEY, J.J. 1983 Equation of motion for a small rigid sphere in a nonuniform flow. *Phys. Fluids* **26** (4), 883–889.
- VAN MINDERHOUT, B., VAN HUIJSTEE, J.C.A., ROMPELBERG, R.M.H., POST, A., PEIJNENBURG, A.T.A., BLOM, P. & BECKERS, J. 2021 Charge of clustered microparticles measured in spatial plasma afterglows follows the smallest enclosing sphere model. *Nat. Commun.* **12** (1), 4692.
- PAN, L. & PADOAN, P. 2010 Relative velocity of inertial particles in turbulent flows. *J. Fluid Mech.* **661**, 73–107.
- PUMIR, A. & WILKINSON, M. 2016 Collisional aggregation due to turbulence. *Annu. Rev. Condens. Matt. Phys.* **7**, 141–170.
- QIAN, X., RUAN, X. & LI, S. 2022 Effect of interparticle dipolar interaction on pore clogging during microfiltration. *Phys. Rev. E* **105** (1), 015102.
- READE, W.C. & COLLINS, L.R. 2000 Effect of preferential concentration on turbulent collision rates. *Phys. Fluids* **12** (10), 2530–2540.
- RUAN, X., CHEN, S. & LI, S. 2021 Effect of long-range coulomb repulsion on adhesive particle agglomeration in homogeneous isotropic turbulence. *J. Fluid Mech.* **915**, A131.
- RUAN, X., GORMAN, M.T., LI, S. & NI, R. 2022 Surface-resolved dynamic simulation of charged non-spherical particles. *J. Comput. Phys.* **466**, 111381.
- RUAN, X. & LI, S. 2022 Effect of electrostatic interaction on impact breakage of agglomerates formed by charged dielectric particles. *Phys. Rev. E* **106** (3), 034905.
- SAW, E.-W., SALAZAR, J.P.L.C., COLLINS, L.R. & SHAW, R.A. 2012 Spatial clustering of polydisperse inertial particles in turbulence. I. Comparing simulation with theory. *New J. Phys.* **14** (10), 105030.
- SHAW, R.A. 2003 Particle-turbulence interactions in atmospheric clouds. *Annu. Rev. Fluid Mech.* **35** (1), 183–227.
- SQUIRES, K.D. & EATON, J.K. 1991 Preferential concentration of particles by turbulence. *Phys. Fluids A* **3** (5), 1169–1178.
- STEINPILZ, T., JOERIS, K., JUNGSMANN, F., WOLF, D., BRENDEL, L., TEISER, J., SHINBROT, T. & WURM, G. 2020 Electrical charging overcomes the bouncing barrier in planet formation. *Nat. Phys.* **16** (2), 225–229.
- SUNDARAM, S. & COLLINS, L.R. 1997 Collision statistics in an isotropic particle-laden turbulent suspension. Part 1. Direct numerical simulations. *J. Fluid Mech.* **335**, 75–109.

Charged bidispersed particles in turbulence

- TOSCHI, F. & BODENSCHATZ, E. 2009 Lagrangian properties of particles in turbulence. *Annu. Rev. Fluid Mech.* **41**, 375–404.
- VAN ATTA, C.W. & ANTONIA, R.A. 1980 Reynolds number dependence of skewness and flatness factors of turbulent velocity derivatives. *Phys. Fluids* **23** (2), 252–257.
- VINCENT, A. & MENEGUZZI, M. 1991 The spatial structure and statistical properties of homogeneous turbulence. *J. Fluid Mech.* **225**, 1–20.
- VOSSKUHLE, M., PUMIR, A., LÉVÊQUE, E. & WILKINSON, M. 2014 Prevalence of the sling effect for enhancing collision rates in turbulent suspensions. *J. Fluid Mech.* **749**, 841–852.
- WAITUKAITIS, S.R., LEE, V., PIERSON, J.M., FORMAN, S.L. & JAEGER, H.M. 2014 Size-dependent same-material tribocharging in insulating grains. *Phys. Rev. Lett.* **112** (21), 218001.
- WANG, L.-P., WEXLER, A.S. & ZHOU, Y. 2000 Statistical mechanical description and modelling of turbulent collision of inertial particles. *J. Fluid Mech.* **415**, 117–153.
- WILKINSON, M. & MEHLIG, B. 2005 Caustics in turbulent aerosols. *Europhys. Lett.* **71** (2), 186.
- WILKINSON, M., MEHLIG, B. & BEZUGLYY, V. 2006 Caustic activation of rain showers. *Phys. Rev. Lett.* **97** (4), 048501.
- YAO, Y. & CAPECELATRO, J. 2018 Competition between drag and coulomb interactions in turbulent particle-laden flows using a coupled-fluid–ewald-summation based approach. *Phys. Rev. Fluids* **3** (3), 034301.
- YEUNG, P.K. & ZHOU, Y. 1997 Universality of the Kolmogorov constant in numerical simulations of turbulence. *Phys. Rev. E* **56** (2), 1746.
- YOSHIMOTO, H. & GOTO, S. 2007 Self-similar clustering of inertial particles in homogeneous turbulence. *J. Fluid Mech.* **577**, 275–286.
- ZHANG, H., CUI, Y. & ZHENG, X. 2023 How electrostatic forces affect particle behaviour in turbulent channel flows. *J. Fluid Mech.* **967**, A8.
- ZHANG, H. & ZHOU, Y.-H. 2020 Reconstructing the electrical structure of dust storms from locally observed electric field data. *Nat. Commun.* **11** (1), 5072.
- ZHAO, K., POMES, F., VOWINCKEL, B., HSU, T.-J., BAI, B. & MEIBURG, E. 2021 Flocculation of suspended cohesive particles in homogeneous isotropic turbulence. *J. Fluid Mech.* **921**, A17.
- ZHOU, Y., WEXLER, A.S. & WANG, L.-P. 2001 Modelling turbulent collision of bidisperse inertial particles. *J. Fluid Mech.* **433**, 77–104.